THE ASTROPHYSICAL JOURNAL, 346:763–772, 1989 November 15


# FORMALDEHYDE ABSORPTION TOWARD W51

A. KOGUT AND G. F. SMOOT
Space Sciences Laboratory and Lawrence Berkeley Laboratory, University of California at Berkeley
AND
C. L. BENNETT AND S. J. PETUCHOWSKI
Laboratory for Astronomy and Solar Physics, NASA Goddard Space Flight Center
*Received 1988 April 21; accepted 1989 May 24*

## ABSTRACT

We have measured formaldehyde ($H_2CO$) absorption toward the H II region complex W51A (G49.5 − 0.4) in the 6 cm and 2 cm wavelength rotational transitions with angular resolution of ~4″ (0.15 pc). The continuum H II region shows a large, previously undetected shell structure 5.5 pc along the major axis. The absorption, converted to optical depth, shows a higher degree of clumping throughout the map than previous maps at lower resolution; in particular, we observe two narrow regions of enhanced opacity. The absorption in the velocity range 64–67 km $s^{-1}$ LSR extends over most of the region, with an observed velocity gradient of 5.2 km $s^{-1}$ $pc^{-1}$. The opacity structure largely parallels the velocity structure, with a ridge of enhanced opacity to the north of the highest velocity feature. The S/N of the maps allows accurate modeling of the spectral profiles. We have identified and parametrized nine distinct clumps in the foreground clouds, and have derived column densities for the $1_{11}$ and $2_{12}$ rotational levels of orthoformaldehyde.

*Subject headings:* interstellar: molecules — nebulae: H II regions — nebulae: individual (W51)

## I. INTRODUCTION

W51 is a giant H II region complex, located in the Sagittarius spiral arm at a distance of ~7.5 kpc (Genzel *et al.* 1981). A number of researchers have studied the radio continuum sources and the associated and foreground molecular clouds. Bieging (1975) has reviewed the morphology of the W51 complex; only a brief overview will be presented here. The W51 complex consists of a number of discrete sources in a diffuse continuum envelope. The brightest of these at wavelength 6 cm is W51A (G49.5 − 0.4). Martin (1972) identified eight components, designated a through h, in the $\lambda = 6$ cm wavelength radio continuum of W51A. Of these, the two brightest (d and e) are associated with near-infrared sources IRS 2 and IRS 1, respectively (Wynn-Williams, Becklin, and Neugebauer 1974; Genzel *et al.* 1982). Scott (1978) has mapped interferometrically the radio continuum about W51d and e, and found two compact sources 1′ to the east of the peak W51e, designated $W51e_1$ and $e_2$. The areas near $W51e_1$, $e_2$, and IRS2 are rich sources of maser activity in OH (Mader, Johnston, and Moran 1978), $H_2O$ (Genzel *et al.* 1982), and of emission from hot $NH_3$ (Mauersberger *et al.* 1987).

Transitions between the low-lying rotational states of orthoformaldehyde are a useful probe of conditions within molecular clouds. W51A has been studied extensively in the $\lambda = 6$ cm wavelength ($1_{10} \leftarrow 1_{11}$) transition (Arnal and Goss 1985; Martin-Pintado *et al.* 1985), and to lower resolution in the $\lambda = 2$ cm wavelength ($2_{11} \leftarrow 2_{12}$) transition (Gardner and Whiteoak 1984), and $\lambda = 2$ mm transitions (Wilson and Jaffe 1981). The results have been used to establish the degree of clumping and turbulence in the absorbing clouds, the local $H_2$ density, and the relative positions of the clouds and continuum sources. The situation is complicated by the extreme projection effects; at Galactic longitude 49°, the line of sight through the Sagittarius spiral arm is nearly 5 kpc.

Comparison of results at different wavelengths has been hampered by differing resolution and sensitivity. As part of a project to measure the temperature of the cosmic microwave background radiation, we have observed $H_2CO$ in absorption at high sensitivity and angular resolution. In this paper, we present new interferometric maps of $H_2CO$ absorption toward W51A, of similar resolution and sensitivity in both the 6 and 2 cm transitions of orthoformaldehyde. We show a new, large shell structure in the continuum to the SW of W51e, apparently connected to the discrete source W51b. The absorption, converted to optical depth, shows significant clumping on the scale of the synthesized beamwidth over most, but not all, of the map.

## II. OBSERVATIONS

The opacity of the absorbing clouds changes rapidly with position across the source. We require high angular resolution measurements in order to minimize opacity fluctuations within a resolution element. To further minimize the effects of small scale density fluctuations, we used equal angular resolution of 4″ at both 6 and 2 cm wavelength, removing the effects of density fluctuations to second order in the ratio of the opacities at the two wavelengths.

We observed the 6 cm transition of orthoformaldehyde (rest frequency 4.8296596 GHz) on 1986 November 8 using the NRAO[1] Very Large Array (VLA) in the C configuration. Spectral coverage consisted of the inner 32 channels of a 256 channel, 3.125 MHz bandpass centered at 65.0 km $s^{-1}$ LSR; the velocity resolution was 0.76 km $s^{-1}$. A total of 5.5 hr was spent on source. We calibrated the flux scale using an assumed value of 7.46 Jy for 3C286, and used a 0.5 hr integration of 3C84 to calibrate the bandpass. Phase calibration used 1923 + 210, observed for 5 minutes of every 30.

We observed the 2 cm transition (rest frequency 14.488479 GHz) on 1987 May 1, 2, and 3, with the VLA in the D configuration. Spectral coverage consisted of the inner 32 channels of

[1] The National Radio Astronomy Observatory is operated by Associated Universities, Inc., under contract with the National Science Foundation.

TABLE 1

OBSERVING PARAMETERS

| Parameter | 6 cm | 2 cm |
|---|---|---|
| Observing dates | 1986 Nov 6 | 1987 May 1, 2, 3 |
| Telescope | VLA, C configuration | VLA, D configuration |
| Number of antennas | 25 | 25 |
| Phase center | | |
| $\alpha_0$(1950.0) | $19^h21^m19^s.0$ | $19^h21^m22^s.5$ |
| $\delta_0$(1950.0) | 14°24′30″ | 14°24′30″ |
| Integration time (h) | 5.5 | 14.5 |
| Primary HPBW | 9′ | 3′ |
| Area mapped ($\alpha \times \delta$) | 8′.5 × 8′.5 | 4′.3 × 4′.3 |
| Synthesized HPBW ($\alpha \times \delta$) | 4″.14 × 3″.59 | 3″.73 × 3″.66 |
| Rest frequency (GHz) | 4.8296596 | 14.488479 |
| Number of channels | 32 | 32 |
| Channel width (kHz) | 12.207 | 24.414 |
| Velocity resolution (km s$^{-1}$) | 0.76 | 0.51 |
| Lowest channel (km s$^{-1}$) | 53.6 | 57.4 |
| Highest channel (km s$^{-1}$) | 76.4 | 72.6 |

a 128 channel, 3.125 MHz bandpass, again centered at 65.0 km s$^{-1}$ LSR, for velocity resolution of 0.51 km s$^{-1}$. A total of 14.5 hr was spent on source, slightly less than expected owing to a power failure at the VLA site on May 3. We calibrated the flux scale using a value for 3C286 of 3.53 Jy. Accurate absolute measurement of the opacity at 2 cm required an accurate determination of the bandpass calibration. We used a 1.5 hr integration of 3C84 (0.5 hr at the end of each of the three observing runs) for bandpass calibration, ensuring that bandpass calibration was not a limiting error in our determination of the absorption spectra. As with the 6 cm observations, we used 1923 + 210, observed 5 minutes of every 30, for phase calibration. Table 1 lists observing parameters for both the 6 cm and 2 cm observations.

## III. DATA REDUCTION

We employed standard VLA calibration and data reduction software to convert the observed visibilities to intensity maps. The three days of 2 cm observation were calibrated independently before being combined into a single visibility data base. The dirty maps were CLEANed and the CLEAN components used as input for self-calibration of the phases.

For either frequency, channel zero contained the average of the inner three-quarters of the originally available passband. The velocity range covered had significant absorption in most channels; these channels formed a nonnegligible fraction of channel zero. Spectra over a wider velocity range (Bieging, Wilson, and Downes 1982) show no absorption features which would have contributed significantly to our channel zero that would not be seen in our 31 spectral channels. Accordingly, we formed a continuum map at both 6 and 2 cm by subtracting from channel zero the suitably weighted average of the 31 data channels. We then applied a correction for primary beam effects, a significant effect at 2 cm where the primary HPBW was approximately the size of the area of interest.

As with any interferometer, the VLA's sensitivity to large-scale structure is determined by the shortest baselines available and the details of the source structure. W51 is known to have considerable extended emission surrounding the compact sources (Bieging, Wilson, and Downes, 1982; Gardner and Whiteoak 1984). Our continuum maps contained 48% and 55%, respectively, of the flux observed by single-dish measurements at 6 and 2 cm wavelength. We added the "missing" flux as a constant across the continuum maps; this amounted to 9.8 mJy beam$^{-1}$ at 6 cm and 17.8 mJy beam$^{-1}$ at 2 cm, effectively raising the zero level of the maps without changing the noise properties. The resultant continuum maps have an RMS noise of 1.5 mJy beam$^{-1}$ at 6 cm, and 3 mJy beam$^{-1}$ at 2 cm, in blank fields near the phase center. The RMS noise rises with increasing distance from the phase center in accordance with the primary beam pattern (Table 1).

We produced dirty maps for each spectral channel, as well as a dirty continuum map (without the corrections described above). All maps were 512″ × 512″ ($\alpha \times \delta$) at 6 cm and 256″ × 256″ at 2 cm, with uniform weighting at both wavelengths to maximize resolution. The absorption maps are the differences between the dirty channel maps and the dirty continuum, CLEANed and corrected for the primary beam pattern. The absorption maps have RMS noise near the phase center of 4 mJy beam$^{-1}$ at 6 cm and 7 mJy beam$^{-1}$ at 2 cm. We then made maps of the optical depth of the formaldehyde lines in the usual fashion. To prevent systematic uncertainties in the subtraction or the continuum from affecting the results, we blanked the optical depth maps wherever corrections to the continuum for missing flux were more than 10% of the continuum. The cutoff level is 100 mJy beam$^{-1}$ for the 6 cm continuum and 75 mJy beam$^{-1}$ at 2 cm.

## IV. RESULTS

### *a) Continuum*

The continuum maps are shown in Figures 1 and 2. It should be emphasized that these maps have had "missing" flux added as a constant across the map, and have been corrected for primary beam attenuation. The rms noise in the original maps, magnified by the correction for primary beam attenuation, appears at the corners of both figures. The first contour of Figure 1 at 10 mJy beam$^{-1}$ corresponds roughly to the zero level of the uncorrected continuum, while the first contour of Figure 2, where rms noise and primary beam correction are larger, is roughly a 4 $\sigma$ contour at 30 mJy beam$^{-1}$.

The 6 cm continuum shows a large, low-level shell structure, not previously observed, which forms a continuation of the elongated compact source W51b. The structure at 6 cm is well above the rms noise (>3 $\sigma$ before adding continuum flux) and does not correspond to the known sidelobe response of the array. It is 2′.5 along the major axis, which, at a distance of 7.5 kpc, corresponds to a linear dimension 5.5 pc. The shell does

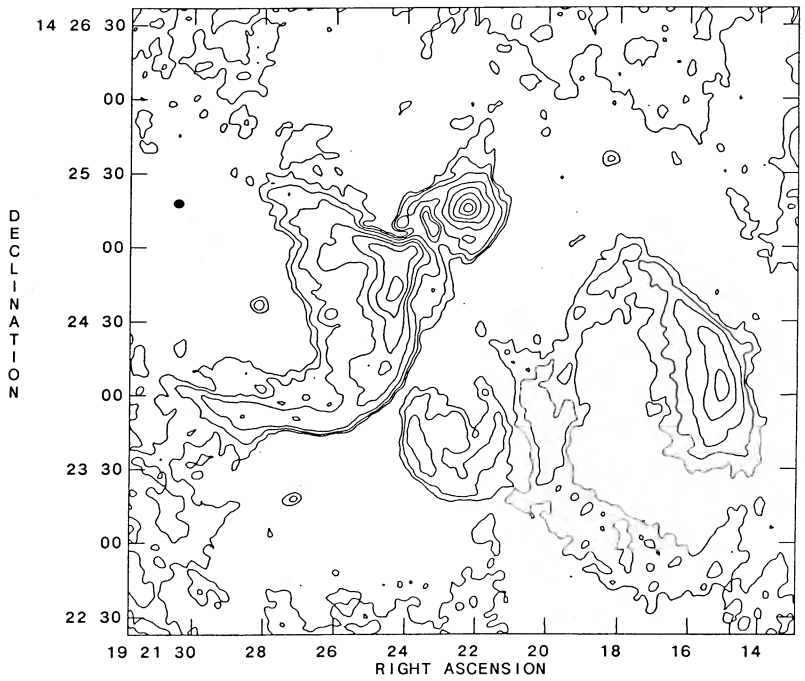


FIG. 1.—The 6 cm wavelength continuum toward W51A (G49.5−0.4). The map has been CLEANed and corrected for the primary beam pattern. Contours are at 10, 20, 40, 100, 200, 400, 800, and 1200 mJy beam$^{-1}$. The beam shape is indicated by the black oval to the upper left.

not show up as clearly in the 2 cm continuum, since it largely lies within 10 mJy beam$^{-1}$ ($\sim 2\ \sigma$, as the shell is near the primary beam half-power point) of the diffuse continuum. Given the relatively low flux density observed at 6 cm, any reasonable spectral index typical of H II regions would place the shell at the limits of detection in our noisier 2 cm continuum map.

Fitted peak intensities for selected features in the continuum maps are shown in Table 2. The ultracompact region W51e$_2$ is visible in both Figures 1 and 2; W51e$_1$, although present in both continuum maps, is not clearly visible in the contoured Figure 1. Neither $e_1$ nor $e_2$ are resolved at either frequency.

### *b) Absorption*

Absorption maps of the d and e features from selected channels are shown in Figures 3 and 4. For clarity, the contour plots have been blanked in regions where the absorption is less than 3 times the RMS noise level. The large changes in absorption from velocities only a few km s$^{-1}$ apart are indicative of the complicated morphology of this region.

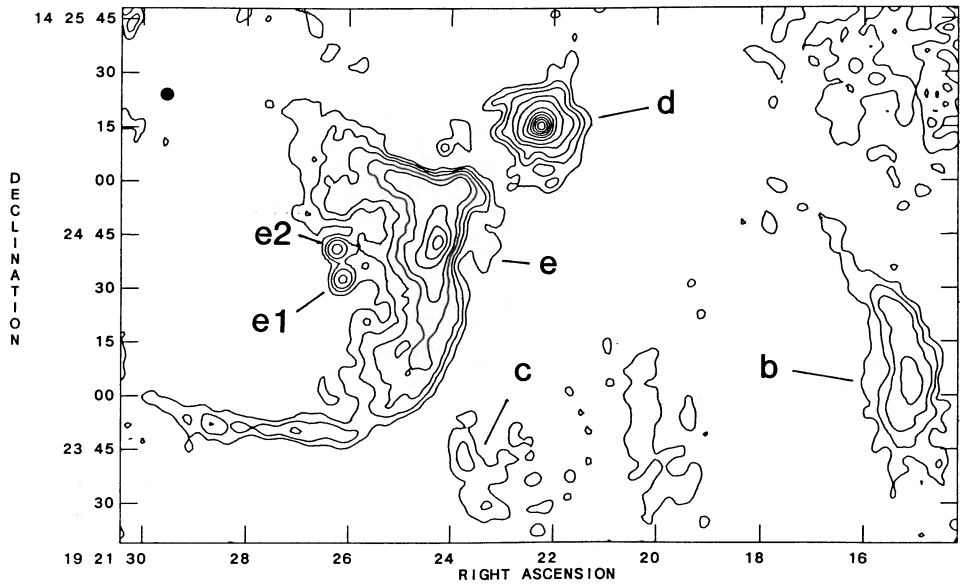


FIG. 2.—The 2 cm wavelength continuum toward W51A. Similar corrections have been applied as for Fig. 1. The first six contours are at 30, 50, 80, 150, 250, and 500 mJy beam$^{-1}$; successive contours are at 300 mJy beam intervals. The designations of Martin (1972) are indicated. The beam size and shape are indicated by the black oval to the upper left.

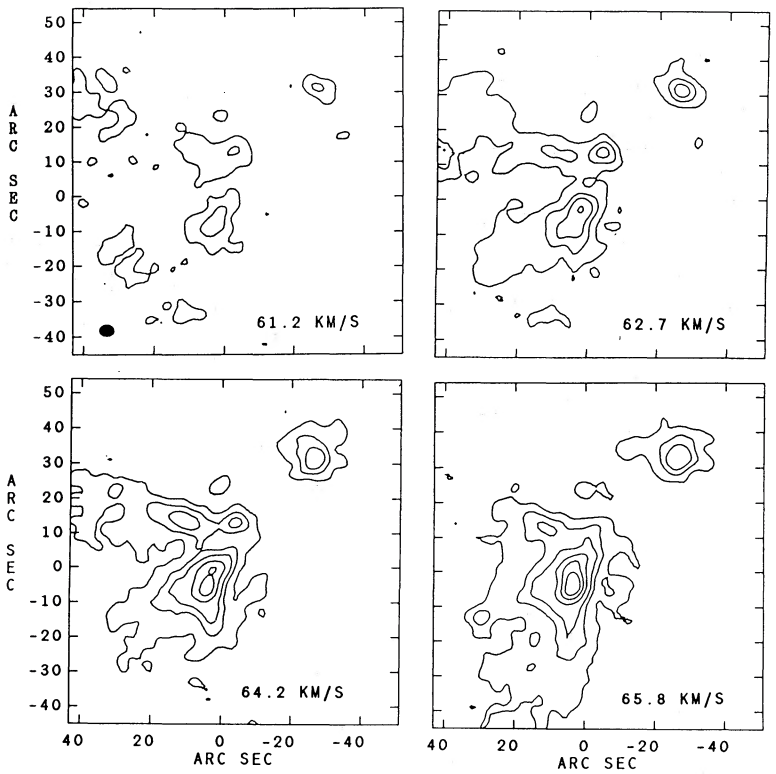


FIG. 3.—Absorption maps at selected channels for the 6 cm wavelength transition. The LSR velocity of each map is indicated. Contours are at 12, 50, 100, 200, 300, and 400 mJy beam$^{-1}$. The plots have been blanked in regions where the absorption is less than 3 times the RMS noise, and have been corrected for the primary beam pattern. The beam size is indicated by the black oval to the lower left. The reference position for Figures 3–8 is at $\alpha = 19^h21^m24^s$, $\delta = 14°24'45''(1950.0)$.

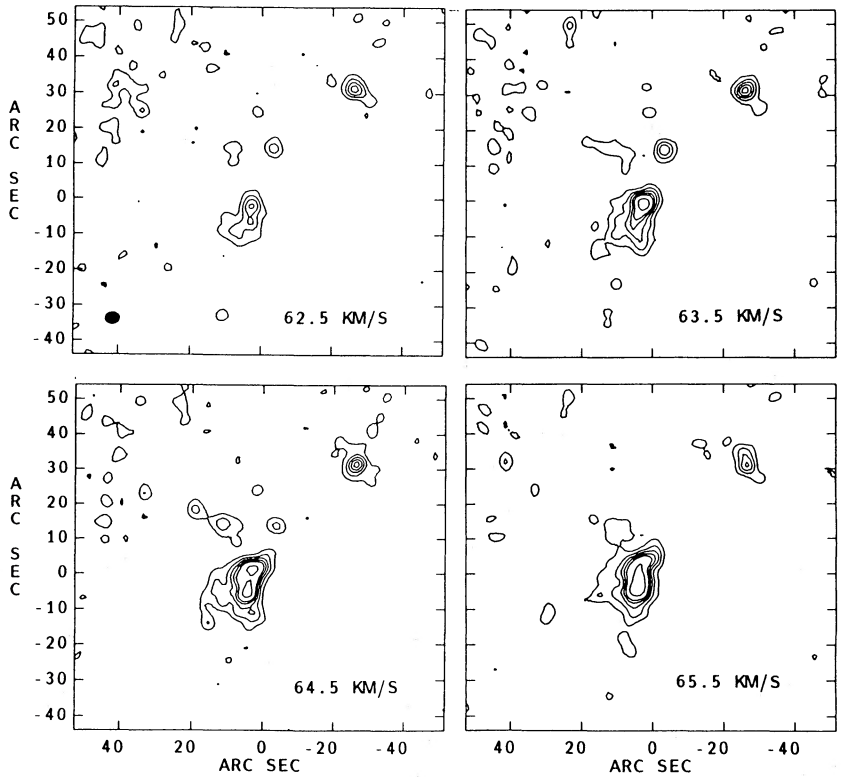


FIG. 4.—Absorption maps at selected channels for the 2 cm wavelength transition. The LSR velocity of each map is indicated in the lower right corner. Contours are at 20, 40, 60, 80, 100, and 150 mJy beam$^{-1}$. The plots have been blanked in regions where the absorption is less than 3 times the rms noise, and have been corrected for the primary beam pattern. The beam size is indicated by the black oval to the lower left.

TABLE 2

CONTINUUM INTENSITY

| FEATURE | PEAK INTENSITY (mJy per beam) 6 cm | 2 cm |
|---|---|---|
| W51d ..... | 1223 ± 16 | 1970 ± 29 |
| W51e ..... | 779 ± 25 | 830 ± 31 |
| W51b ..... | 198 ± 5 | 162 ± 3 |
| $W51e_1$ .... | 125 ± 9 | 155 ± 6 |
| $W51e_2$ .... | 48 ± 4 | 177 ± 6 |

We observe no regions where formaldehyde is in emission. Although the cm-wavelength transitions thermalize under conditions of very high $H_2$ density ($n_{H2} > 10^6$ cm$^{-3}$), and could conceivably appear in emission in regions where the diffuse continuum emission is weak, the absorption maps show no significant emission features. The limit derived is fairly weak (2 cm emission features $< 5$ K at 95% confidence), corresponding to a kinetic temperature $< 46$ K for the typical opacities ($\sim 0.15$) found in the 2 cm absorption spectra. If the centimeter wavelength transitions are not thermalized, no emission would be expected.

*c) Optical Depth*

Contour plots of the optical depth in selected channels toward W51d and W51e are presented in Figures 5 and 6. We have blanked the maps in areas in which corrections to the continuum for "missing" flux amount to more than 10% of the uncorrected intensity. The large opacities seen at the edges of the continuum region are thus unlikely to be artifacts of the mapping process.

Although several regions show relatively small, smooth variations, the observed opacity is dominated by clumping on angular scales of the beamwidth (4″), corresponding to linear scales of 0.15 pc. The opacity increases to the E of W51e and to the N and NW of W51d, in qualitative agreement with the results of Arnal and Goss (1985) and Martin-Pintado *et al.* (1985). In general, we derive higher opacity in the clump peaks, as would be expected for our finer angular resolution in the present of clumping. A new feature in our maps is the concentration of the largest opacities in extended, ridged features, particularly near 66 and 69.5 km s$^{-1}$ toward W51e. These features are narrow N-S (on the order of the synthesized beamwidth), and extend roughly E-W across the entire background continuum source. The opacity enhancements in these features are large; the opacity at 69 km s$^{-1}$ varies from 0.71 to

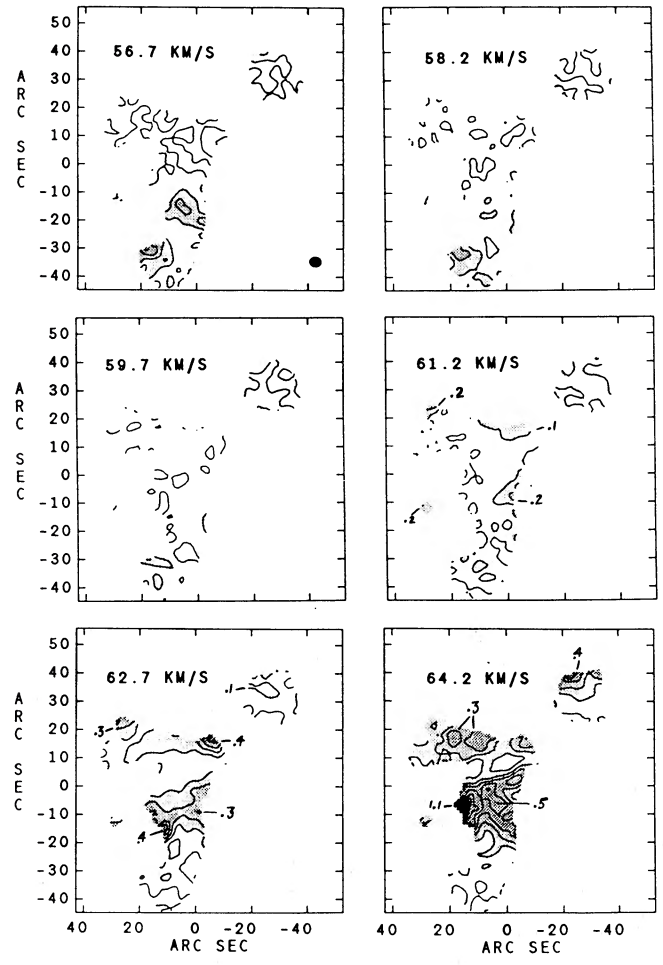


FIG. 5a

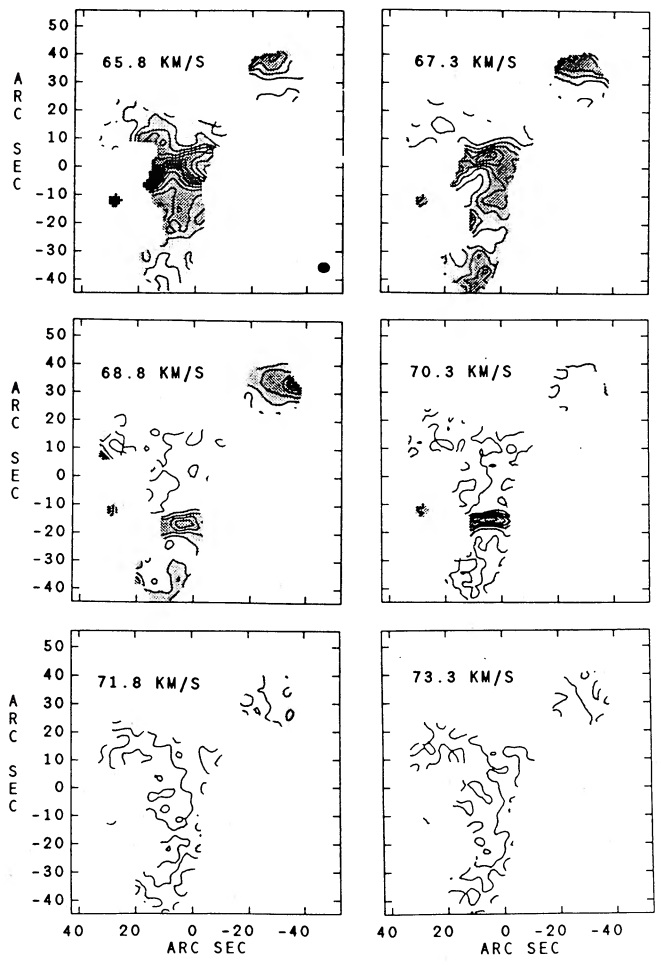


FIG. 5b

FIG. 5.—(*a–b*) Maps of the optical depth in selected channels of the 6 cm transition. The LSR velocity of each plot is indicated in the upper left corner. The lowest contour is at 0.0 opacity; successive contours are spaced by 0.1 to a maximum of 1.2. The gray scale distinguishes regions of increasing and decreasing opacity; selected contours are labeled. The beam size is indicated by the shaded oval at the bottom right corner of the first plot.

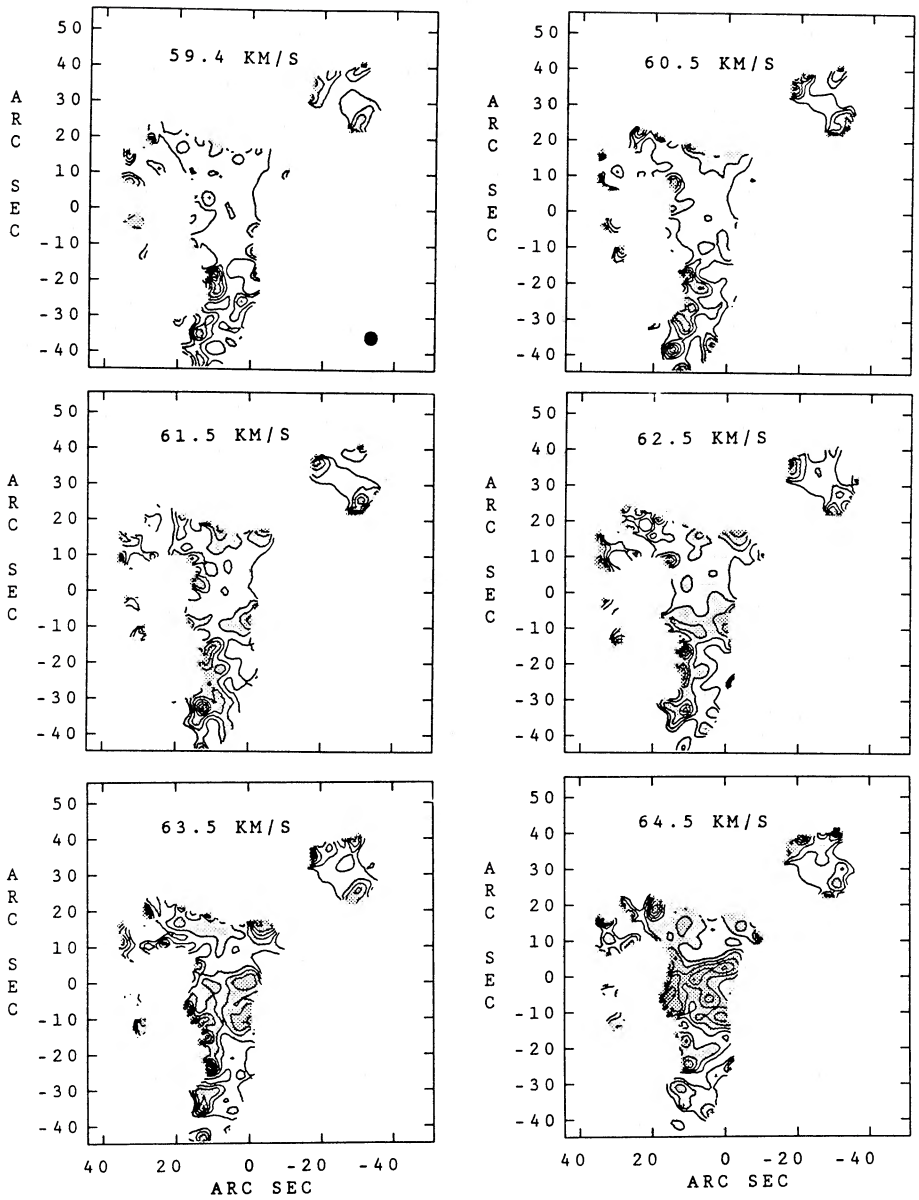


FIG. 6*a*

FIG. 6.—(*a–b*) Maps of the optical depth in selected channels of the 2 cm transition. The LSR velocity of each plot is indicated in the upper left corner. The lowest contour is at 0.0 opacity; successive contours are spaced by 0.05 to a maximum of 0.6. The beam size is indicated by the shaded oval at the bottom right corner of the first plot.

0.15 in a single beamwidth at 6 cm. The linear extent E-W is fairly large, at least 1.3 pc (the extent of the illuminating background).

Both ridged structures correspond to regions toward W51e that show the largest extended velocity gradients. We have fitted Gaussian profiles to the opacity spectra at each pixel of the channel maps, using two Gaussians in regions where this significantly improved the fit to the data. The FWHM of the spectra is typically $\sim$2.5 km s$^{-1}$ (several channels); we find that several superposed features often contribute to the opacity seen in a given location and channel. The S/N of our data allows deconvolution of the complicated spatial and velocity structure of the absorbing clouds. Figure 7 shows the fitted velocities as a function of declination for several strips across the clouds. Each pixel on the declination axis has been fitted to one or two spectral features. The northern half of W51e exhibits a smooth velocity gradient of 5.2 km s$^{-1}$ pc$^{-1}$ from 64 to 66.8 km s$^{-1}$, falling back to 65 km s$^{-1}$ further south. The feature at 69 km s$^{-1}$ in the southern half of W51e shows a smooth gradient of 6.0 km s$^{-1}$ pc$^{-1}$, falling from 69.8 to 68.3 km s$^{-1}$. The opacity from 64–67 km s$^{-1}$ extends over most of the source and can be seen in superposition beneath the 69 km s$^{-1}$ feature. The southernmost region of W51e shows an extended region (0.5 pc) at 67.5 km s$^{-1}$ without significant velocity gradients.

The opacity of the ridged structure at 66 km s$^{-1}$ is correlated with the velocity structure of the clouds. In Figure 8*a* we have plotted the opacity in the velocity range 63–67 km s$^{-1}$. Figure 8*b* shows the fitted velocity centroid of the opacity at each pixel; at pixels with two spectral features, the velocity

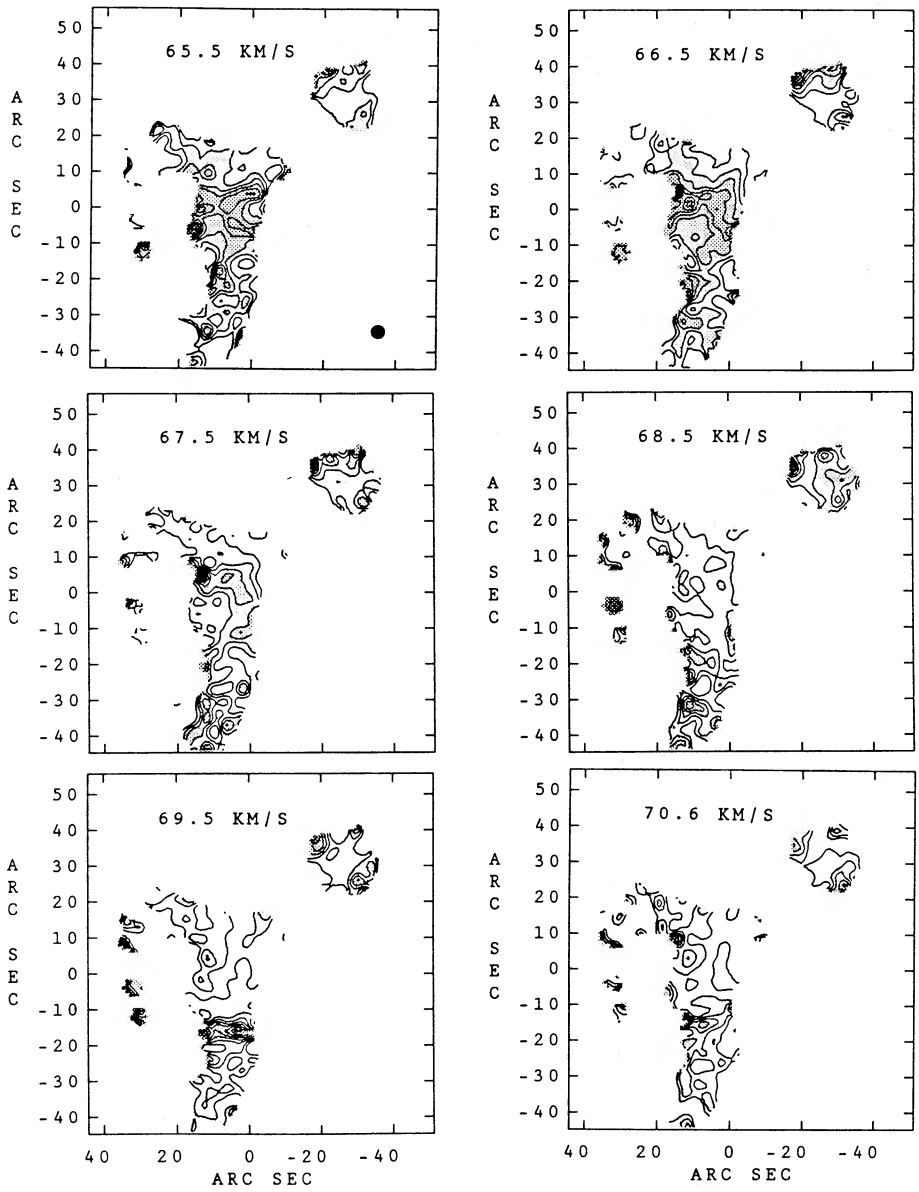


FIG. 6b

corresponding to the feature with the larger opacity is shown. The velocity gradient across the northern half of W51e is clearly visible. Both the velocity and the opacity structure toward the northern half of W51e contain a bifurcated structure extended NE–SW across the source. The regions of highest velocity ($\sim$66.7 km s$^{-1}$) lie consistently 1″–6″ north of the regions of highest opacity. The highest opacity enhancements are at a velocity of 65 km s$^{-1}$, $\sim$1.5 km s$^{-1}$ lower than the peak velocity of the cloud.

By contrast, the opacity seen toward the continuum source W51d shows two spectral features with smooth opacity gradients and little clumping (Figs. 5 and 6). The denser opacity feature at 68.4 km s$^{-1}$ shows an extended velocity gradient of 6.8 km s$^{-1}$ pc$^{-1}$ at the eastern edge of W51d, but is flat across the rest of the source (Fig. 7). The weaker feature at 64–66 km s$^{-1}$ shows a more complicated velocity structure, characterized by flat profiles separated by fairly sharp gradients of 12 km s$^{-1}$ pc$^{-1}$ toward the center of the source. These velocity profiles change dramatically between strips one beamwidth apart, indicative of the complicated morphology of the clouds.

## V. DISCUSSION

We have used the fitted spectra at each pixel to isolate a number of "clumps" of enhanced opacity. Given sufficient S/N, this provides a better estimate of the opacity of each clump than would the original spectral cubes, which are subject to spillover from wide spectral features in nearby channels. We isolated the clumps using the following algorithm. First, we generated a map of opacity versus position for all pixels containing absorption with fitted velocities in a range defined by the separation of the features. Toward W51d, cuts at 63–66.5 and 67–69.5 km s$^{-1}$ served to separate the two spectral features. Toward W51e, where the morphology was more complicated, we used cuts at 61–63, 63–67, 66.5–68, and 67.5–70 km

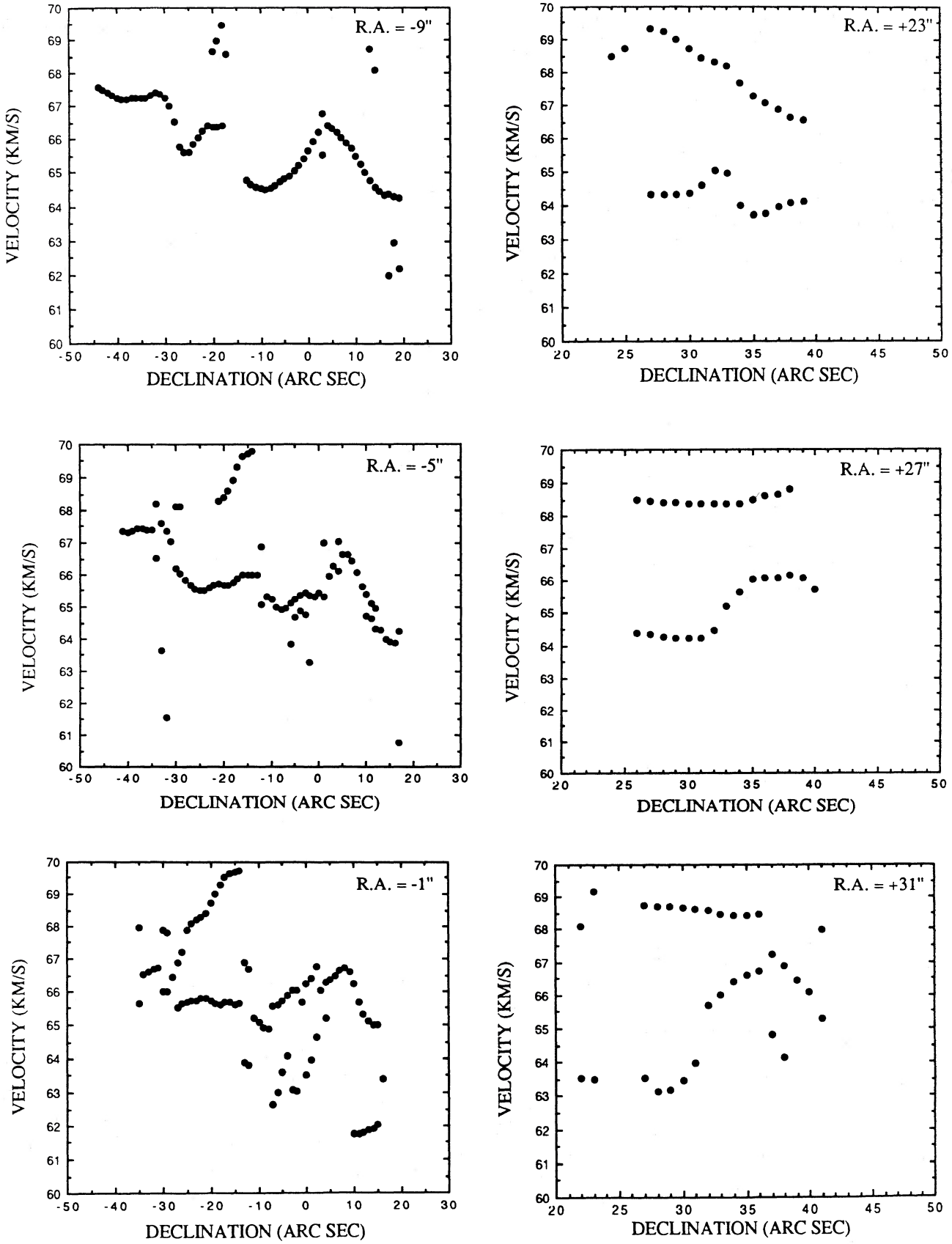


FIG. 7.—Velocity centroids of the fitted 6 cm spectra plotted vs. declination for selected strips toward W51e and W51d. The axis reference positions are the same as Fig. 3.

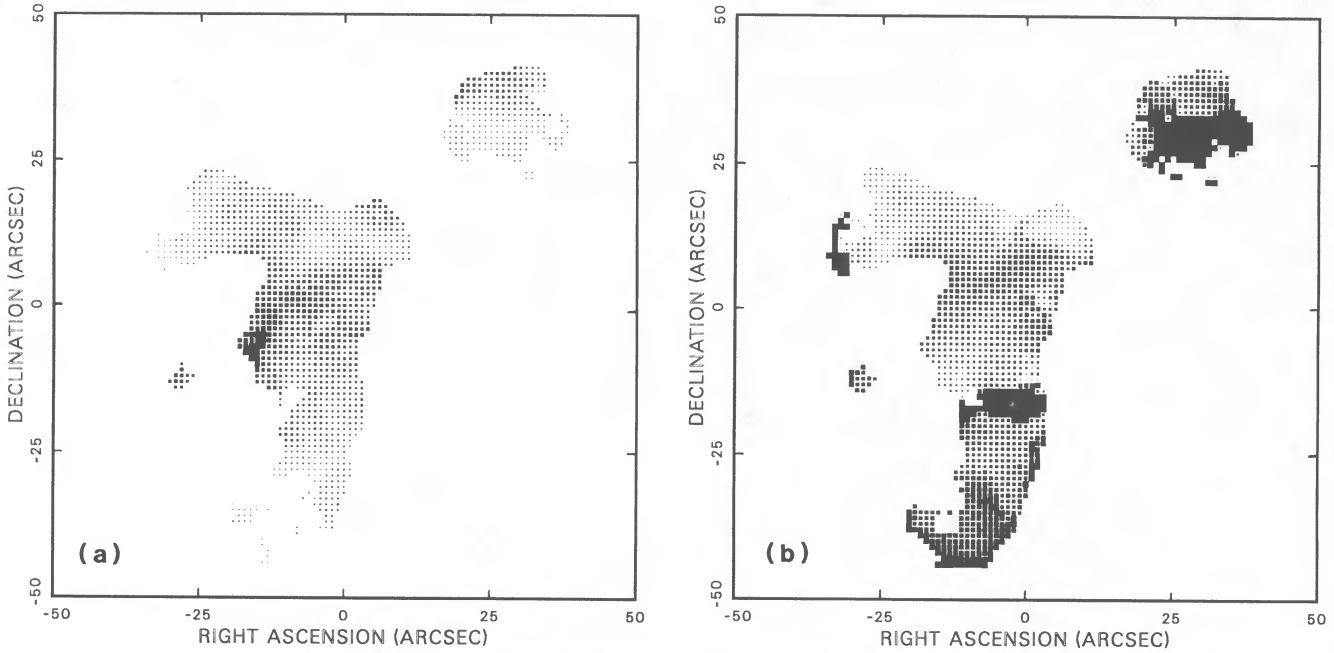


FIG. 8.—(*a*) The fitted opacity for all pixels showing absorption between 63 and 67 km $s^{-1}$, plotted vs. position. The opacity gray scale runs from 0.0 (white) to 1.0 (black). (*b*) The velocity of the fitted opacity plotted vs. position. For locations with two velocity features, the one corresponding to the larger opacity is shown. The velocity gray scale runs from 63 km $s^{-1}$ (smallest dot) to 68 km $s^{-1}$ (black). The axis reference positions are the same as Fig. 3.

$s^{-1}$. We then took as clump candidates those pixels with opacity enhancement greater than 50% over surrounding areas and rejected any consisting of fewer than 8 contiguous pixels ($\sim$0.5 of the synthesized beam area). We then compared the cuts at 6 cm and 2 cm, and rejected any candidates which did not appear at the same location at both frequencies. This last test served to reject noisy data, but does introduce a bias against weak opacity features, which may not appear in the noisier 2 cm spectra.

Table 3 summarizes the properties of the clumps. It is not intended as an exhaustive list of all cloud condensations toward W51A, but summarizes the properties of those clumps meeting our criteria. All data are taken for the pixel at clump center, with the largest opacity enhancement. The velocity, FWHM, and opacity at 6 cm and 2 cm are taken from Gaussian spectra fitted to the data. The uncertainties are calculated by comparing the fitted spectra to the data, using scatter in several "blank" channels at either end of the 31 channel passband to estimate the noise in each opacity spectrum. Systematic uncertainties from such factors as uncertainty in the continuum owing to "missing" flux density in the interferometric maps have not been explicitly included in these error estimates. An uncertainty of 50% in the added flux contributes less than 5% uncertainty to the optical depths presented; the effect largely cancels in comparison of the 6 cm and 2 cm results. The opacity has 50% variations over regions separated by one to two beamwidths; we have thus not subtracted any "ambient" or diffuse component from the observed clump opacities.

We have converted the optical depth to $H_2CO$ column density $N_1$ in the lower ($1_{11}$) level of the 6 cm transition using the relation

$$\int \tau_{6\ \mathrm{cm}}\, dv = \frac{8\pi^3}{6h} |\mu_{6\ \mathrm{cm}}|^2\, N_1 \left[1 - \exp\left(\frac{-h\nu_{6\ \mathrm{cm}}}{kT_{6\ \mathrm{cm}}}\right)\right], \quad (1)$$

where $\mu_{6\ \mathrm{cm}}$ is the dipole transition moment of the 6 cm transition, $\nu$ is the frequency, $T_{6\ \mathrm{cm}}$ is the excitation temperature of the 6 cm transition, $h$ is Planck's constant, and $k$ is Boltzmann's constant. The integrated opacities are calculated from

TABLE 3

SUMMARY OF OPACITY SPECTRA

| CLUMP (1) | $\alpha$ (1950.0) (2) | $\delta$ (1950.0) (3) | $V$ (km $s^{-1}$) (4) | FWHM (km $s^{-1}$) (5) | OPTICAL DEPTH 6 cm (6) | OPTICAL DEPTH 2 cm (7) | $N_1$ ($10^{13}$ $cm^{-2}$ $K^{-1}$) (8) | $N_2$ ($10^{13}$ $cm^{-2}$ $K^{-1}$) (9) |
|---|---|---|---|---|---|---|---|---|
| 1..... | $19^h21^m24^s.93$ | 14°24′39″ | 65.1 | 2.66 ± 0.05 | 1.004 ± 0.014 | 0.335 ± 0.017 | 3.59 ± 0.08 | 1.20 ± 0.06 |
| 2..... | 19 21 24.20 | 14 24 38 | 65.1 | 3.53 ± 0.05 | 0.585 ± 0.007 | 0.192 ± 0.008 | 2.78 ± 0.05 | 0.91 ± 0.04 |
| 3..... | 19 21 23.73 | 14 24 49 | 65.7 | 3.62 ± 0.07 | 0.509 ± 0.007 | 0.228 ± 0.018 | 2.48 ± 0.06 | 1.11 ± 0.09 |
| 4..... | 19 21 24.67 | 14 24 58 | 64.7 | 3.29 ± 0.09 | 0.374 ± 0.008 | 0.103 ± 0.011 | 1.65 ± 0.06 | 0.46 ± 0.05 |
| 5..... | 19 21 25.27 | 14 25 1 | 64.3 | 2.49 ± 0.19 | 0.343 ± 0.022 | 0.160 ± 0.025 | 1.15 ± 0.11 | 0.54 ± 0.09 |
| 6..... | 19 21 22.20 | 14 25 24 | 65.7 | 3.71 ± 0.21 | 0.501 ± 0.023 | 0.173 ± 0.045 | 2.50 ± 0.18 | 0.86 ± 0.23 |
| 7..... | 19 21 21.53 | 14 25 17 | 68.7 | 1.88 ± 0.21 | 0.536 ± 0.031 | 0.290 ± 0.045 | 1.35 ± 0.17 | 0.73 ± 0.14 |
| 8..... | 19 21 24.07 | 14 24 28 | 69.6 | 1.62 ± 0.09 | 0.714 ± 0.032 | 0.379 ± 0.030 | 1.55 ± 0.11 | 0.83 ± 0.08 |
| 9..... | 19 21 24.40 | 14 24 7 | 67.4 | 2.47 ± 0.16 | 0.364 ± 0.019 | 0.129 ± 0.028 | 1.21 ± 0.10 | 0.43 ± 0.10 |

the fitted spectra; the column densities in two transitions are shown in Table 3. There is generally excellent agreement between the velocity centroids and widths in the two transitions; we use the more sensitive 6 cm FWHM for the integration over velocity in equation (1). At moderate $H_2$ densities ($10^2 \leq n \leq 10^5$ cm$^{-3}$), collisional pumping reduces the excitation temperatures $T_{6\ \mathrm{cm}}$ and $T_{2\ \mathrm{cm}}$ to subthermal values, typically 1.7–2.5 K (Garrison *et al.* 1975). Since there is no accurate estimation of these temperatures toward W51, the temperature dependence has been left explicit in the column densities in Table 3. No correction has been made for beam effects on clumps of size comparable to the beamwidth.

Estimates of local conditions in the clump ($H_2CO$ and $H_2$ density, mm wavelength excitation temperature) may be calculated from the opacity spectra, but are subject to uncertainty in a number of assumptions (e.g., spherical symmetry, temperature of the cm-wavelength transitions, collisional excitation). In a forthcoming paper (Kogut *et al.* 1989), we will present estimates of the hydrogen density and the 2 mm wavelength excitation temperatures in the absorbing clouds toward W51A, using the 6 and 2 cm wavelength opacities from this paper.

## VI. CONCLUSIONS

We have mapped the absorption of orthoformaldehyde toward W51A in both the 6 cm and 2 cm wavelength transitions. The source shows a complicated morphology, including a large, dim shell structure in the continuum and patchy, highly clumped absorption. The absorbing clouds are clumped on scales down to the beamwidth (0.15 pc); the largest opacities observed form extended narrow ridges across the source. The extended ridge of enhanced opacity at 66 km s$^{-1}$ is correlated with and lies $\sim$0.15 pc S of similar structure in the velocity of the clouds. The absorption in the range 64–67 km s$^{-1}$ covers the entire region, but is highly clumped toward the continuum region W51e while exhibiting only a smooth opacity gradient toward W51d 30″ away. Absorption at 67–70 km s$^{-1}$ is patchy.

We have identified and parameterized nine condensations ("clumps") in the absorbing clouds. We derive the column densities for the $1_{11}$ and $2_{12}$ rotational levels of orthoformaldehyde for each of the clumps.

We thank M. Goss and J. Van Gorkom for useful advice at the VLA. H. Liszt (NRAO) provided help using CLEAN algorithms on sources containing both bright regions and diffuse continuum. The VLA array operators proved quite resourceful in enabling us to take data after a power outage damaged a number of the controlling computers. Partial funding for this project has been provided by DOE contract DEAC03-76-SF00098, NASA contract NAS5-27592, and NASA RTOP 188-41-55-07.

## REFERENCES

Arnal, E. M., and Goss, W. M. 1985, *Astr. Ap.*, **145**, 369.
Bieging, J. 1975, in *H II regions and Related Topics*, ed. T. L. Wilson, and D. Downes (Berlin: Springer-Verlag), p. 443.
Bieging, J., Wilson, T. L., and Downes, D. 1982, *Astr. Ap. Suppl. Ser.*, **49**, 607.
Gardner, F. F., and Whiteoak, J. B. 1984, *M.N.R.A.S.*, **210**, 23.
Garrison, B. J., Lester, W. A., Jr., Miller, W. H., and Green, S. 1975, *Ap. J. (Letters)*, **200**, L175.
Genzel, R., *et al.* 1981, *Ap. J.*, **247**, 1039.
———. 1982, *Ap. J.*, **255**, 527.
Kogut, A., Smoot, G. F., Bennett, C. L., and Petuchowski, S. J. 1989, in preparation.
Mader, G. L., Johnston, K. J., and Moran, J. M. 1978, *Ap. J.*, **224**, 115.
Martin, A. H. M. 1972, *M.N.R.A.S.*, **157**, 31.
Martin-Pintado, J., Wilson, T. L., Johnston, K. J., and Henkel, C. 1985. *Ap. J.*, **299**, 386.
Mauersberger, R., Henkel, C., and Wilson, T. L. 1987, *Astr. Ap.*, **173**, 352.
Scott, P. F. 1978, *M.N.R.A.S.*, **183**, 435.
Wilson, T. L., and Jaffe, D. T. 1981, *Ap. J.*, **245**, 866.
Wynn-Williams, C. G., Becklin, E. E., and Neugebauer, G. 1974, *Ap. J.*, **187**, 473.

C. L. Bennett and S. J. Petuchowski: Code 685, Laboratory for Astronomy and Solar Physics, NASA Goddard Space Flight Center, Greenbelt, MD 20771

A. Kogut and G. F. Smoot: 50/232 Lawrence Berkeley Laboratory, University of California, Berkeley, CA 94720